Materials Science-Poland, 34(2), 2016, pp. 266-274
http://www.materialsscience.pwr.wroc.pl/
DOI: 10.1515/msp-2016-0045

DE GRUYTER OPEN

Characterization of NiO–Al_2O_3 composite and its conductivity in biogas for solid oxide fuel cell

SARIKA P. PATIL[1], L.D. JADHAV[2,*], D.P. DUBAL[3], V.R. PURI[1]

[1]Department of Physics, Shivaji University, Kolhapur, India-416004
[2]Electrochemical Energy Materials Laboratory, Department of Physics, Rajaram College, Kolhapur, India-416004
[3]Catalan Institute of Nanoscience and Nanotechnology, Campus UAB, Spain

NiO–Al_2O_3 nanocomposite has been synthesized by mixing combustion synthesized powders. The nanocomposite is an effective anode/anode functional layer for intermediate temperature solid oxide fuel cells. The TEM of NiO and Al_2O_3 revealed spherical particles of 30 nm and platelets of 70 nm, respectively. The XRD analysis of NiO–Al_2O_3 composite sintered at 900 °C showed presence of cubic NiO and rhombohedral α-Al_2O_3 which were chemically stable. However, above 1200 °C $NiAl_2O_4$ started to appear. The conductivity of NiO–Al_2O_3 was the highest in hydrogen (4.3×10^{-3} S/cm at 600 °C). In biogas, the conductivity was 3.2×10^{-3} S/cm with the activation energy of 0.67 eV. The stability of the composite in biogas was also examined.

Keywords: *oxides; chemical synthesis; X-ray diffraction; electrical conductivity; microstructure*

1. Introduction

Ni–Al_2O_3 composite is a very useful, low-cost functional material with high catalytic activity and high mechanical performance [1, 2]. Therefore, it has widely been used in various industrial processes [3–6]. Furthermore, these composites have also developed renewed interest in their partial applications in CO_2 reduction [7, 8], as a protective barrier, as electrochromic materials in smart windows [9], in sensors [10] as surface layers and in toughening processes [11].

Steam reforming of hydrocarbons to form hydrogen has been considered as a potential way to produce a fuel for solid oxide fuel cells (SOFCs). The high temperature (700 °C to 1100 °C) of steam reforming requires robust catalyst and α-Al_2O_3 is the best option. Moreover, Ni–Al_2O_3 has been used as an active and selective catalyst for dry CO_2 reforming of methane [12]. Thus, the superior catalytic properties together with effectiveness in preventing coke formation over the anode layer suggest using Ni–Al_2O_3 as anode/anode functional layer (AFL) in SOFC operating on methane fuel. It exhibits better performance compared to Ni-YSZ [13].

Moreover, Li et al. [14] reported M–Al_2O_3 cermet supported tubular SOFC by thermal spraying while Hoboken [15] reported flame sprayed Ni–Al_2O_3 wherein cermet coating played a dual role as a support tube and an anode current collector. The cell with the Ni–Al_2O_3 catalyst layer showed significant improvement in performance, operating on both pure methane and methane oxygen mixtures of the gases. Furthermore, the cell performance deterioration rate was also greatly reduced even when operating on pure methane fuel [16]. In a real fuel cell, the Ni–Al_2O_3 catalyst layer effectively protects the anode from coke formation, especially for the region near to the anode-electrolyte interface, where the electrochemically active sites are mainly located. Besides, Eguchi et al. [13] reported that the Ni–Al_2O_3 catalyst absorbs much more hydrogen, than the Ni-YSZ composite below 950 °C, which would be beneficial to the catalytic activity of electrode reaction:

*E-mail: ldjadhav.phy@gmail.com

$$H_2 \rightarrow 2H^+ + 2e^- \quad (1)$$

The Ni–Al system shows higher creep resistance compared with the conventional Ni anodes. Further, the presence of Al_2O_3 may increase the surface area of the NiO accompanied by an increase in the catalytic and chemisorptive activity of NiO.

In view of the catalytic activity of NiO–Al_2O_3 for hydrocarbons, we here propose it as an anode material for hydrocarbon based intermediate temperature solid oxide fuel cells. The nanopowders of NiO and α-Al_2O_3 were obtained by solution combustion and were mixed physically to get a composite. The benefits of solution combustion are low cost, simplicity and fast response, fast heating rates and short reaction times as compared to other techniques, such as sol gel method [17], wet impregnation techniques [18], etc. The process of combustion gives homogeneous, crystalline and un-agglomerated multi-component oxide ceramic powder [19]. The composite was characterized by different techniques, such as XRD, SEM, and EDS. The DC conductivity of the pellets was measured in different atmospheres. Here, the CO_2 reforming of methane by NiO–Al_2O_3 was also explored by measuring DC conductivity in biogas, whose main constituents were methane and CO_2.

2. Experimental

2.1. Sample preparation

Metal nitrates were used as an oxidizer and glycine as a fuel for the combustion synthesis. Pure chemicals, $Ni(NO_3)_2{\cdot}6H_2O$, Al $(NO_3)_3{\cdot}9H_2O$, and $C_2H_5NO_2$ (glycine) of analytical grade, all from Alfa Aesar were used. The stoichiometric composition of the redox mixture was calculated based on the principles of propellant chemistry, keeping the O/F ratio around unity [20]. The chemicals in required amounts were dissolved in double distilled water. The intimate solution of metal nitrate and glycine was obtained using a magnetic stirrer with heating to evaporate the excess water content in the solution. After formation of gel, it was kept in preheated furnace (600 °C) where it was auto-ignited with the rapid evolution of large volume of gases to produce fine powder. Assuming complete combustion, the chemical reactions at optimum oxidant to fuel ratio are as given below:

$$Ni(NO_3)_2 6H_2O + 1.11C_2H_5NO_2 \xrightarrow{\Delta 300\,C} NiO + 2.22CO_2\uparrow + 8.78H_2O\uparrow + 1.56N_2\uparrow + 0.0025O_2\uparrow \quad (2)$$

and

$$2[Al(NO_3)_3 9H_2O] + 3.32C_2H_5NO_2 \xrightarrow{\Delta 300\,C} Al_2O_3 + 6.64CO_2\uparrow + 26.3H_2O\uparrow + 4.66N_2\uparrow + 0.03O_2\uparrow \quad (3)$$

Within a very short duration, the local reaction temperature rose from 1200 °C to 1500 °C as it was confirmed by an infrared pyrometer. The adiabatic flame temperatures were calculated using equation 4 [21] and the thermodynamic data have been collected in Table 1:

$$T_{ad} = 298 + \frac{(-\Delta H^o)}{\sum (nCp)} \quad (4)$$

The calculated values of the adiabatic flame temperatures are 978 °C for NiO and 1323 °C for α-Al_2O_3, respectively.

The as-obtained NiO and Al_2O_3 powders were heat treated at 600 and 1200 °C for 2 h to remove any type of carboneous impurity and hence, pure and well crystalline powders were obtained. The heat treated powders (30 % NiO and 70 % α-Al_2O_3) were further physically mixed and pelletized in circular shapes. The pellets were sintered at different temperatures.

Structural studies of the samples were carried out by XRD (Phillips-3710 powder X-ray diffractometer) in the 2θ range of 10 to 90° using Cu$K\alpha_1$ radiation (λ = 1.54056 Å). The morphology of the powder was studied using scanning electron microscopy (SEM, JEOL JSM-6360). The particle size of a sample prepared at stoichiometric ratio was studied with a transmission electron microscope (TEM, PHILIPS CM200). The DC conductivity of sintered pellets was measured in air, hydrogen and biogas atmospheres in the temperature range from room temperature to 600 °C. The

Table 1. Calculations of adiabatic flame temperature.

Compound	ΔH_f [Kcal/mol]	Cp [Kcal/mol K] at 298 K
$Ni(NO_3)_2\ 6H_2O$	−528.6	–
$Al(NO_3)_3\ 9H_2O$	−857.59	–
$C_2H_5NO_2$	−126.22	–
NiO	−57.3	0.01059
α-Al_2O_3	−399.09	0.01889
CO_2	−94.05	0.00887
N_2	–	0.00696
H_2O	−57.97	0.00803
O_2	–	0.00701
Adiabatic flame temperature of NiO		978 °C
Adiabatic flame temperature of α-Al_2O_3		1323 °C

data were collected during cooling to ensure temperature stabilization and to avoid any change due to in-situ reduction of surface during heating. The NiO–Al_2O_3 was screen printed on both sides of pre-sintered NiO-GDC and its conductivity was evaluated as anode functional layer.

A complete cell was formed by using NiO-GDC, GDC and LSCF-GDC as anode, electrolyte and cathode, respectively and NiO–Al_2O_3 as anode functional layer. The open circuit voltages (OCV) of the cells were also measured in biogas.

3. Results and discussion

3.1. Powder characterization

The X-ray diffraction patterns of as-synthesized and calcined powders of NiO and α-Al_2O_3 nanoparticles are shown in Fig. 1 and Fig. 2, respectively. Fig. 1a depicts the XRD pattern of as-obtained NiO, which shows peaks arising from NiO and also nickel nitrate, indicating that combustion is incomplete. The combustion of this residual occurs during subsequent calcination at 600 °C for 2 h and phase pure cubic NiO is obtained (Fig. 1b). The calcined powder has crystallites of 31 nm and lattice parameter of 4.17 Å.

On the other hand, the as-obtained Al_2O_3 is amorphous (Fig. 2a). It needs high calcination temperature to obtain crystalline α-Al_2O_3 particles. Therefore, the as-obtained powder was calcined at

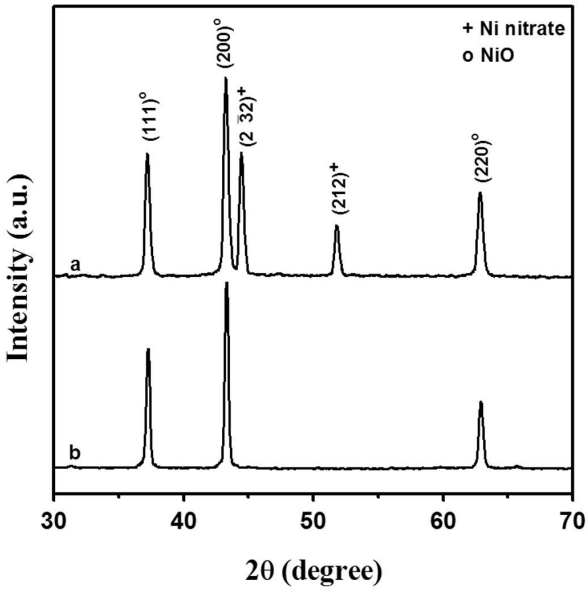

Fig. 1. XRD patterns of NiO nanoparticles (a) as prepared and (b) calcined at 600 °C.

1200 °C for 2 h. Its XRD pattern (Fig. 2b) shows broad peaks indicating presence of small size particles (∼34 nm). The α-Al_2O_3 nanoparticles have crystallized into the rhombohedral structure with lattice parameters; a = b = 4.76 Å and c = 12.76 Å. The elemental analysis of the calcined powders also showed the peaks due to either Ni and oxygen or Al and oxygen. No impurities were detected. The analysis data are tabulated in Table 2.

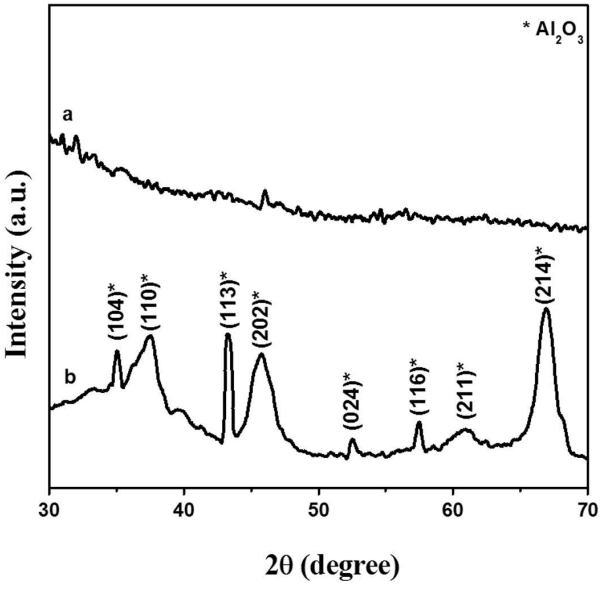

Fig. 2. XRD patterns of α-Al_2O_3 nanoparticles (a) as prepared and (b) calcined at 1200 °C.

Table 2. Elemental analysis of NiO and Al_2O_3.

Atomic % of NiO	Ni	54.43
	O	45.57
Atomic % of Al_2O_3	Al	37.90
	O	62.10

The morphology of the as-obtained (Fig. 3a) and calcined (Fig. 3b) NiO powder shows almost the same features and is foam-like with highly porous structure. The porosity has little decreased after calcination. The insets in the figures reveal roughly spherical grains. The TEM image of NiO nanoparticles (Fig. 3c) shows the nearly spherical particles, 30 nm in size. The SEM images of the as-obtained and calcined Al_2O_3 nanoparticles are shown in Fig. 4a and 4b. The amorphous-like structure without well-defined particle shapes is observable from SEM image of as-obtained Al_2O_3 (Fig. 4a). The amorphous powder is constituted of micrograins with a large size distribution. After calcination, the grain growth occurs and highly silky soft powder is seen in the SEM image (Fig. 4b). The higher magnified image of α-Al_2O_3 is shown in the inset of Fig. 4b. It reveals the platelet

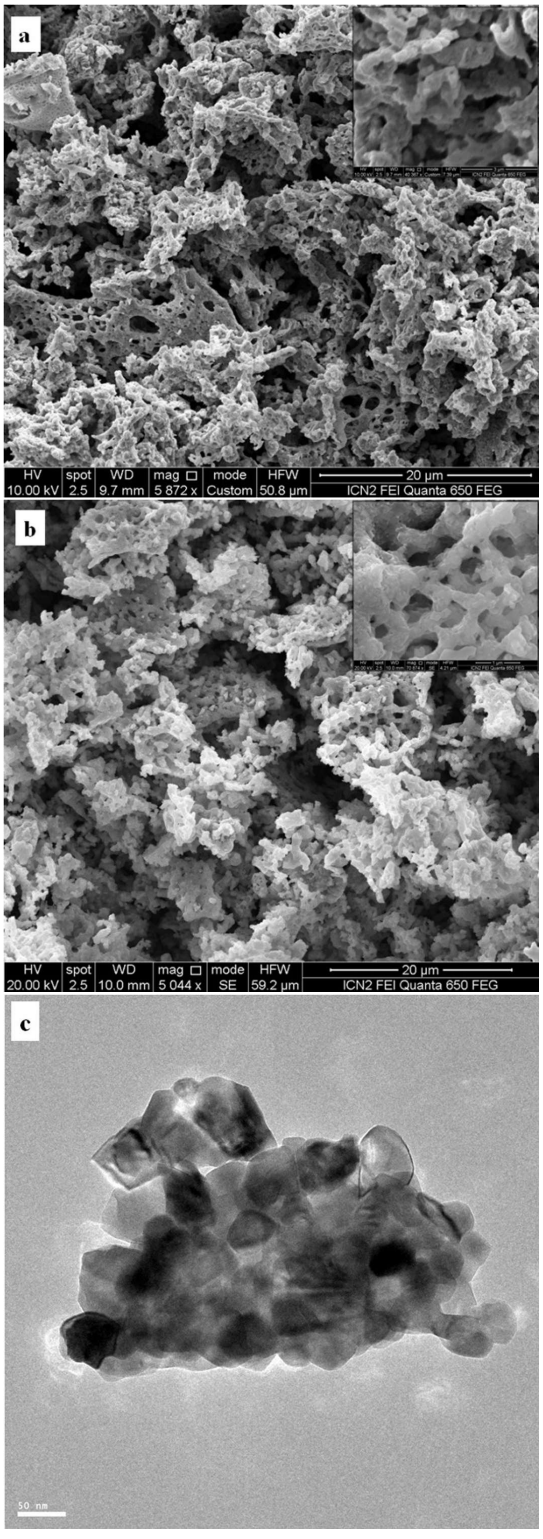

Fig. 3. SEM images of (a) as prepared (b) calcined and (c) TEM image of as prepared NiO nanoparticles. The inset shows images obtained at higher magnification.

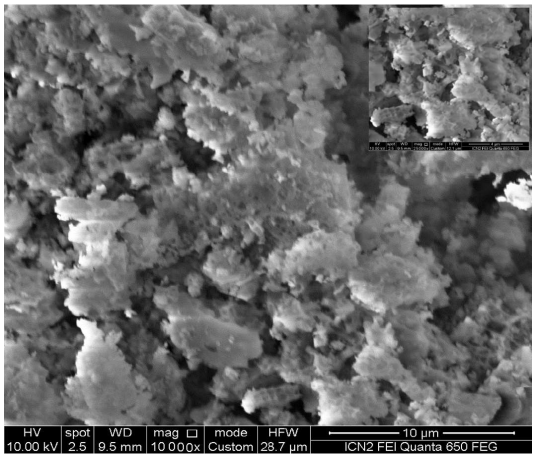

(a)

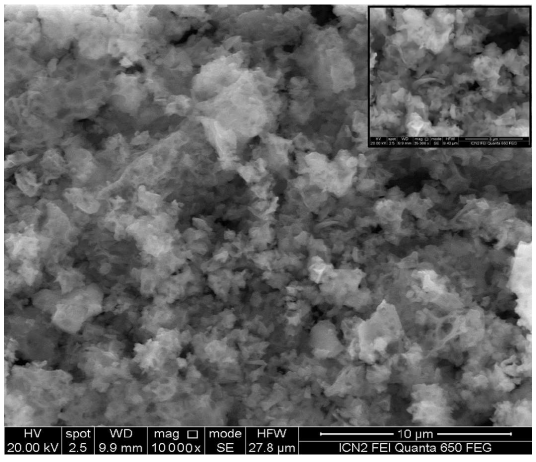

(b)

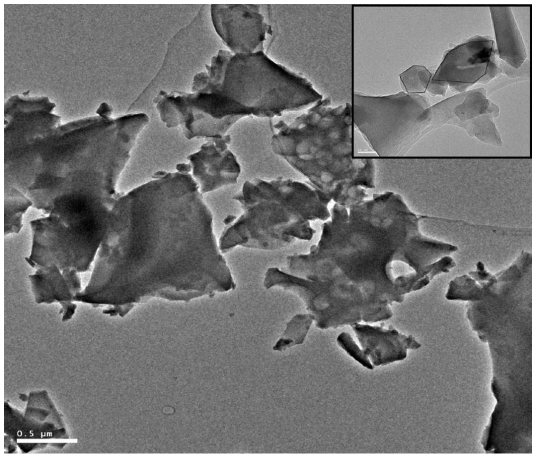

(c)

Fig. 4. SEM images of (a) as prepared (b) calcined and (c) TEM image of as-prepared α-Al_2O_3 nanoparticles. The inset shows images obtained at higher magnification.

morphology of α-Al_2O_3. The TEM of Al_2O_3 (Fig. 4c) shows a mixture of different kinds of particles: platelets, spherical and needles but most crystallites exhibit hexagonal platelet morphology as shown in the inset of Fig. 4c. The average size of the platelet is 70 nm.

3.2. Ni–Al_2O_3 nanocomposite

The green pellets of NiO–Al_2O_3 were finally sintered at 900 °C and 1200 °C for 2 h and their structural evaluation is shown in Fig. 5a and Fig. 5b. It is observed that the peaks from cubic NiO and rhombohedral α-Al_2O_3 overlap appreciably. The diffraction peaks in 2θ range of 60° to 70° show presence of peaks at 63.21° and 67.08° corresponding to NiO and Al_2O_3, which undoubtedly evidence the absence of $NiAl_2O_4$. Thus, no intermediate phases are formed in the composite sintered at 900 °C, which suggests no solid solution among α-Al_2O_3 and NiO. However, higher sintering temperature (1200 °C) results in intermediate $NiAl_2O_4$ spinel phase as shown in Fig. 5b. The sharp intense peaks indicate that the material is in crystalline form, but the crystallite sizes have not improved considerably. They are in the range of 33 nm to 35 nm for NiO and 37 nm to 40 nm for α-Al_2O_3.

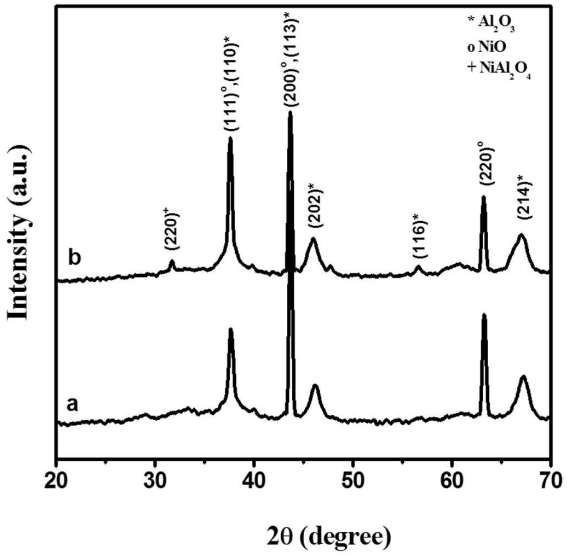

Fig. 5. XRD patterns of NiO–Al_2O_3 nanocomposite sintered at (a) 900 °C and (b) 1200 °C.

The presence of $NiAl_2O_4$ in the composite sintered at 1200 °C for 2 h is calculated by using following formula:

$$\text{Percent phase intensity} = \frac{I_{NiAl_2O_4}(220)}{I_{NiAl_2O_4}(220) + I_{NiO}(200) + I_{Al_2O_3}(113)} \text{X}\,100 \quad (5)$$

It is seen that only about 3 % spinel is present in the NiO–Al_2O_3 composite. The lattice parameters of α-Al_2O_3 and NiO phases are collected in Table 3.

On the contrary, Wang et al. [22] observed that Ni loading up to 20 wt.% was soluble in Al_2O_3 forming spinel $NiAl_2O_4$, and NiO loading above 20 % formed Ni–Al_2O_3. This shows that NiO species reacted with the Al_2O_3 to form a spinel $NiAl_2O_4$ phase. Moreover, Hao et al. [23] reported that the NiO phase started to appear in Ni–Al_2O_3 prepared by an aerogel method at nickel contents exceeding about 20 wt.%. These results indicate that the degree of reaction between nickel and the Al_2O_3 in the Ni–Al_2O_3 catalysts is dependent on the preparation method.

The EDS analysis of NiO–Al_2O_3 nanocomposite shows that the atomic percent of Ni in the pellets sintered at 900 °C and 1200 °C is 22.99 and 19.51, respectively, contrary to the theoretically expected value of 17.65. This demonstrates slight inhomogeneous distribution of Ni. Similarly, the atomic percent of Al in the pellets sintered at 900 °C and 1200 °C is 77 and 80.49, respectively, contrary to the theoretically expected value of 82.35.

SEM images of NiO–Al_2O_3 nanocomposites are shown in the Fig. 6. Fig. 6a reflects non uniform grain distribution with poor crystalline structure in the sample sintered at 900 °C. It exhibits platelet like structures and it is composed of Al_2O_3 as observed in Fig. 4b. After sintering at 1200 °C, the grain growth is observed and spherically shaped pores appear.

The DC conductivity of NiO–Al_2O_3 was measured in the temperature range of 200 °C to 610 °C. The plots of DC conductivity (σ) versus reciprocal

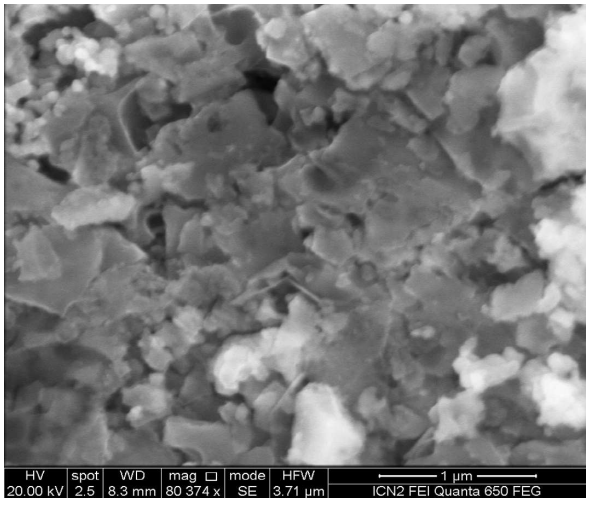

(a)

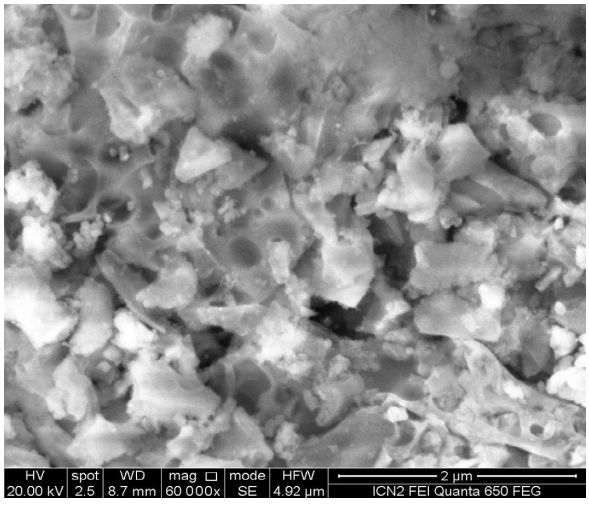

(b)

Fig. 6. SEM images of NiO–Al_2O_3 nanocomposite sintered at (a) 900 °C and (b) 1200 °C.

of temperature in air, hydrogen and biogas atmospheres are shown in the Fig. 7. The conductivity is observed to increase with temperature, suggesting thermally activated process. One can observe that the lowest conductivity values are found in air in the whole studied temperature range. Four times enhancement of the conductivity occurs in hydrogen. Further, the conductivity in air and biogas is almost the same up to 380 °C.

In air, initiation of ionic conduction due to hopping of oxide ions is observed above 415 °C while electronic conductivity is negligible. In hydrogen,

Table 3. The lattice parameters and crystallite size of NiO and α-Al_2O_3 phases in the composite.

Material NiO–Al_2O_3 nanocomposite	Lattice parameter [Å] NiO a	α-Al_2O_3 a = b	α-Al_2O_3 c	Crystallite size [nm] NiO	α-Al_2O_3
Standard data	4.17	4.75	12.99		
Sintered at 900 °C	4.15	4.75	12.85	34	35
Sintered at 1200 °C	4.15	4.76	12.88	37	37

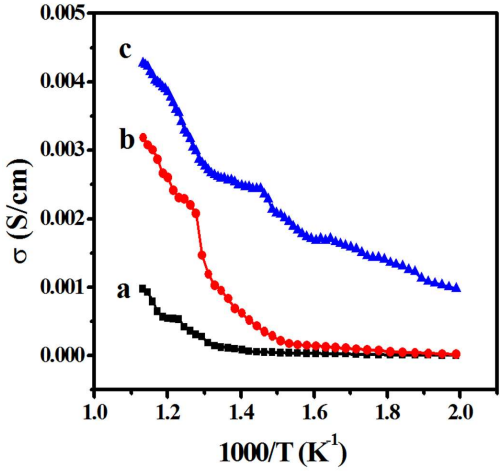

Fig. 7. DC conductivity of NiO–Al_2O_3 in (a) air, (b) biogas and (c) hydrogen atmosphere.

due to the catalytic activity of NiO, it gets oxidized to protons and electrons (equation 1). These electrons are effectively transported by electronic phase (NiO) in the composite. This gives high conductivity with the least activation energy of 0.23 eV. The catalytic reactivity is improved with a rise in temperature giving a considerable increase in conductivity. The slight change in the slope of conductivity is attributable to the change in defect mechanism.

On the contrary, in biogas, substantial increase in conductivity above 415 °C is observed. The biogas being a mixture of CH_4 and CO_2, undergoes dry reformation by NiO–Al_2O_3 according to reaction:

$$CH_4 + CO_2 \rightarrow 2CO + 2H_2 \qquad (6)$$

A little amount of air has also been introduced during the measurements giving partial oxidation of CH_4 according to reaction:

$$CH_4 + \frac{1}{2}O_2 \rightarrow CO + 2H_2 \qquad (7)$$

In addition, NiO–Al_2O_3 oxidizes the hydrogen obtained in this processes and plays a dual role. However, the comparatively less conductivity in biogas than in hydrogen and high activation energy of 0.67 eV signify that a less quantity of hydrogen is available. Nonetheless, propensity of CO_2 cracking may also be the reason of this lower conductivity. The conductivity and activation energy values in different atmospheres are tabulated in Table 4.

The FT-IR spectra of NiO–Al_2O_3 exposed in biogas at 400 °C, 500 °C and 600 °C for 2 h are shown in Fig. 8a. All the spectra show broad bands in the region 3000 to 3700 cm^{-1} and a strong band at 2341 cm^{-1}. The bands near 3000 cm^{-1} are assigned to C–H stretching vibrations (from methane) and those around 3500 cm^{-1} are due to presence of moisture. The band at 2341 cm^{-1} is due to asymmetric stretching vibration of C=O (CO_2). The intensity of this band is observed to decrease with the temperature. The band at 864 cm^{-1} is observed to shift to 890 cm^{-1} and then to 989 cm^{-1} with an increase in temperature, shifting the M–O vibrations to higher wave number side.

Moreover, the bands in the region 1300 to 1800 cm^{-1} are observed for the anode exposed at 400 °C and 500 °C. These are due to CH_4 adsorbed on the surface. This band disappears at 600 °C and two distinct peaks, attributed to O–H vibrations and vibrations of adsorbed water molecule are observed at 1343 cm^{-1} and 1543 cm^{-1}, respectively. The water molecules originate from the cracking of CO formed in reaction 6 and 7 by reaction:

$$CO + H_2 \rightarrow C + H_2O \qquad (8)$$

Table 4. DC conductivity and activation energy values in different atmospheres.

Materials	Atmosphere	Conductivity [S/cm] × 10^{-3}	Activation energy [eV] 400 °C to 610 °C
NiO–Al_2O_3	Air	0.97	0.88
	Biogas	3.2	0.67
	Hydrogen	4.3	0.23

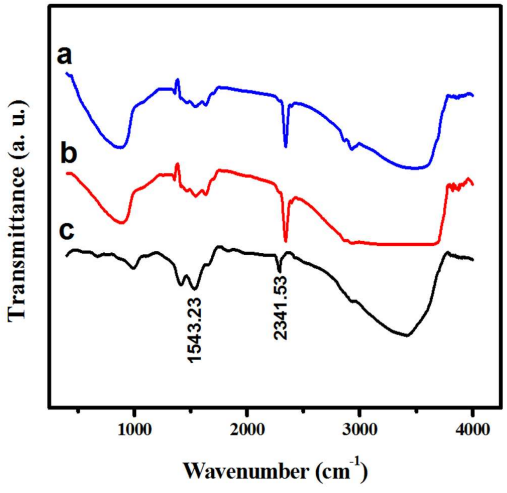

(a)

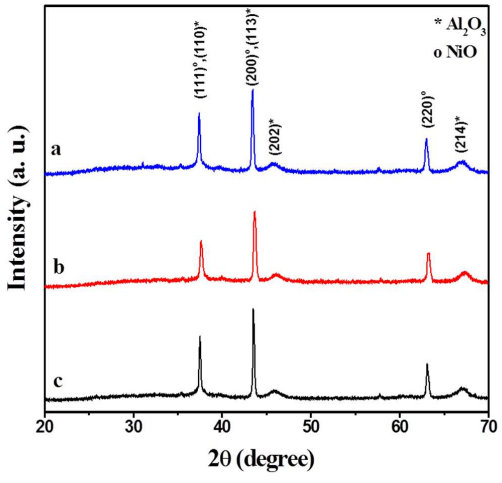

(b)

Fig. 8. (a) FT-IR and (b) XRD patterns of NiO–Al_2O_3 after exposure to biogas at (a) 400 °C, (b) 500 °C, and (c) 600 °C temperatures.

If this is the case, carbon would be present in the sample but it has not been detected in XRD. This is because carbon is very sensitive to water in the atmosphere. Hence, it forms O–H functional groups showing a band at 1343 cm^{-1}. Thus, the analysis of FT-IR spectra clearly shows the presence of surface adsorbed CH_4 and CO_2 at 400 °C and 500 °C. Generally, biogas contains methane (50 % to 70 %), carbon dioxide (30 % to 40 %) and other compounds such as hydrogen sulfide (in ppm), water, and other trace gas compounds. The H_2S is easily soluble in water. The absorption process is purely physical. Therefore, sulfur is not deposited on the surface of the material and has not been detected by FT-IR spectroscopy.

The XRD patterns of the samples exposed to biogas at temperatures of 400 °C, 500 °C, and 600 °C are shown in Fig. 8b. It shows all the peaks corresponding to NiO and α-Al_2O_3. Further, no Ni peaks have been observed what means that reduction of NiO has not occurred.

The OCV of single cells NiO-GDC/GDC/LSCF-GDC and NiO–Al_2O_3–NiO-GDC/GDC/LSCF-GDC were measured in biogas at 500 °C. The OCV of a cell formed with NiO-GDC anode was 0.64 V while that of NiO–Al_2O_3–NiO-GDC anode was 1.11 V, close to the theoretical value of 1.18 V.

4. Conclusions

In conclusion, the NiO–Al_2O_3 nanocomposite for anode in IT-SOFCs has been successfully synthesized. The composite without any intermediate phase like $NiAl_2O_4$ was obtained at 900 °C. The conductivity in hydrogen was 4.3 × 10^{-3} S/cm with the least activation energy of 0.23 eV, which suggests that NiO–Al_2O_3 catalyzes hydrogen effectively. Moreover, conductivity in biogas was slightly less, with the activation energy of 0.67 eV. The higher activation energy implies that NiO–Al_2O_3 has to play a dual role

of reforming biogas followed by oxidation of hydrogen. Further, the lower availability of hydrogen and propensity of CO_2 cracking may also be the reason of this lower conductivity. FT-IR showed presence of CH_4 and CO_2 adsorbed on the anode surface at 400 °C and 500 °C, but not at 600 °C. The OCV of NiO–Al_2O_3–NiO-GDC/GDC/LSCF-GDC single cell in biogas atmosphere is 1.11 V at 500 °C. Hence, NiO–Al_2O_3 anode material can be considered as a potential candidate for use in hydrocarbon fueled SOFCs.

Acknowledgements

One of the authors, Ms. S.P. Patil, is very much thankful to Rohit Gore, the Ferguson College, Pune, for providing characterization facilities and the Department of Physics, the Shivaji University, Kolhapur, for providing XRD facilities.

References

[1] READMAN J.E., OLAFSEN A., SMITH J.B., BLOM R., *Energ. Fuel*, 20 (2006), 1382.
[2] JOHANSSON E., MATTISSON T., LYNGFELT A., THUNMAN H., *Fuel*, 85 (2006), 1428.
[3] KAEWPUANG S., INAZU K., KOBAYASHI T., AIKA K., *Water Res.*, 38 (2004), 778.
[4] AZURDIA J.A., MARCHAL J., SHEA P., SUN H., PAN X.Q., LAINE R.M., *Chem. Mater.*, 18 (2006), 731.
[5] ZHANG X., LIU J., JING Y., XIE Y., *Appl. Catal.*, 240 (2003), 143.
[6] CHOKKARAM S., SRINIVASAN R., MILBURN D.R., DAVIS B.H., *J. Mol. Catal. A-Chem.*, 121 (1997), 157.
[7] CHOI J.S., MOON K.I., KIM Y.G., LEE J.S., KIM C.H., TRIMM D.L., *Catal. Lett.*, 52 (1998), 43.
[8] FEI J.H., HOU Z.Y., ZHENG X.M., YASHIMA T.S., *Catal. Lett.*, 98 (2004), 241.
[9] AVENDANO E., AZENS A., NIKLASSON G.A., GRANQVIST C.G., *Sol. Energ. Mat. Sol. C.*, 84 (2004), 337.
[10] VIJAYA J.J., KENNEDY L.J., SEKARAN G., NAGARAJA K.S., *Mater. Lett.*, 61 (2007), 5213.
[11] ABE O., TAKATA S., OHWA Y., *J. Eur. Ceram. Soc.*, 24 (2004), 489.
[12] CHEN Y.Z., SHAO Z.P., XU N.P., *Energ. Fuel*, 22 (2008), 1873.
[13] EGUCHI K., KUNISA Y., KAYANO M., SEKIZAWA K., YANO S., ARAI H., *Denki Kagaku*, 64 (1996), 596.
[14] LI C., LI C., XING Y., XIE Y., LONG H., *Rare Metals*, 25 (2006), 273.
[15] HOBOKEN N.J., *J. Therm. Spray Techn.*, 16 (2007), 306.
[16] WANG W., ZHOU W., RAN R., CAI R., SHAO Z.P., *Electrochem. Commun.*, 11 (2009), 194.
[17] TAO S., ZHAN Z., MENG G., *J. Mater. Sci. Lett.*, 18 (1999), 707.
[18] FA L., HUI X., DONG-MEI Z., WAN-CHENG Z., *T. Nonferr. Metal Soc.*, 17 (2007), 1400.
[19] JADHAV L.D., PATIL S.P., CHAVAN A.U., JAMALE A.P., PURI V.R., *Micro Nano Lett.*, 6 (2011), 812.
[20] JADHAV L.D., PATIL S.P., JAMALE A.P., CHAVAN A.U., *Mater. Sci. Forum*, 757 (2013), 85.
[21] JADHAV L.D., CHOURASHIYA M.G., JAMALE A.P., CHAVAN A.U., PATIL S.P., *J. Alloy. Compd.*, 506 (2010), 739.
[22] WANG W., RAN R., SU C., SHAO Z., JUNG D., SEO W.S., LEE S.M., *Int. J. Hydrogen Energ.*, 36 (2011), 10958.
[23] HAO Z.G., ZHU Q.S., JIANG Z., HOU B.L., LI H.Z., *Int. J. Hydrogen Energ.*, 90 (2009), 113.

Received 2015-04-24
Accepted 2016-02-17